Materials Research. 2019; 22(3): e20180446
DOI: http://dx.doi.org/10.1590/1980-5373-MR-2018-0446

Structural, Morphological and Magnetic Properties of FeCo-$(Fe,Co)_3O_4$ Nanocomposite Synthesized by Proteic Sol-Gel Method Using a Rotary Oven

***Diego Felix Dias*[a], *Tiago Pinheiro Braga*[b]*, *João Maria Soares*[c], *José Marcos Sasaki*[a]**

[a]*Laboratório de Raios X, Departamento de Física, Universidade Federal do Ceará, Fortaleza, CE, Brasil*
[b]*Laboratório de Peneiras Moleculares (LABPEMOL), Instituto de Química, Universidade Federal do Rio Grande do Norte, Natal, RN, Brasil*
[c]*Departamento de Física, Universidade do Estado do Rio Grande do Norte, Mossoró, RN, Brasil*

Received: June 25, 2018; Revised: January 22, 2019; Accepted: February 15, 2019

FeCo nanoparticles coated with $(Fe,Co)_3O_4$ (magnetite doped with cobalt) were synthesized by the proteic sol-gel chemical route. The synthesized materials were characterized by Thermogravimetry (TG), X-Ray Diffraction (XRD), Scanning Electron Microscopy (SEM), Transmission Electron Microscopy (TEM), vibrating-sample magnetometer (VSM) and Mössbauer spectroscopy (MS). The results show that the increase in temperature and the choice of the correct air/N_2 flow directly influence on the final physical-chemical properties of the nanocomposite. The SEM and TEM images confirmed that a thin layer of oxide was formed on the alloy, indicating that it was obtained a self-assembled FeCo-$(Fe,Co)_3O_4$ nanocomposites. In addition, the VSM results show that a possible exchange-spring coupling in magnetic FeCo-$(Fe,Co)_3O_4$ nanoparticles occurred with high saturation magnetization from FeCo alloy and high coercivity from $(Fe,Co)_3O_4$. The rotary oven allows the uniform contact of the powder with the atmosphere of synthesis during the different oxidation-reduction steps, generating more homogeneous particles.

Keywords: *Nanocomposite, FeCo-$(Fe,Co)_3O_4$, Rotary Oven and Proteic Sol-Gel.*

1. Introduction

A great attention has been given to a class of solids named nanocomposites, containing multicomponent hybrid nanostructures with two or more nanosized constituents assembled in a controlled way [1,2]. Nanocomposite solids have been studied extensively since it is possible to obtain properties which cannot be acquired with the isolated phases. Different types of composites have been prepared due to their mechanical, structural, chemical, morphological and magnetic properties which are usually different compared to each phase taken alone. These advantages make nanocomposites one of the most promising candidates for the exploration of new applications compared to isolated solids containing a single phase [3-7].

Several methods are being used for the synthesis of composite materials such as mechanical alloying, reduction of oxides in gels, infiltration techniques, high-energy ball milling, reduction, decomposition of metallic precursors in polymers, among others [8-12]. Nanocomposites containing specifically FeCo alloy and Co-containing Fe_3O_4 is rarely presented in the literature, however, some articles show the synthesis in aqueous medium under hydrothermal conditions [12,13].

In this work, a synthetic route was developed based on proteic sol-gel method (gelatin). The functional groups of the gelatin (amino and carboxylic acid) may act as an excellent complexing agent of metallic cations such as Fe^{3+}or Co^{2+}, which is very interesting during the synthesis of metal oxide and alloy with high metallic dispersion, since the gelatine allows a uniform dispersion of the cations during the formation of the hybrid material (xerogel) and minimizes sintering during the calcination step favoring the formation of nanoparticles [6]. It is important to emphasize that interesting results have already been presented in the synthesis of the magnetite and FeCo alloy isolated using the protein sol-gel method [14,15], however, the synthesis of self-assembled FeCo-$(Fe,Co)_3O_4$ nanocomposites has not yet been explored using this synthetic route and needs to be studied to confirm its viability. In this case, the nanocomposite will be composed of FeCo alloy and $(Co,Fe)_3O_4$ (Co containing magnetite).

These materials were chosen due to their magnetic properties are different. The FeCo alloy is a material with several unique characteristics such as high curie temperature, high mechanical strength and is a soft magnetic solid (has a high saturation magnetization and low coercivity) [16-25]. On the other hand, magnetite is a hard magnetic material, presenting a low saturation magnetization and a high coercivity [26]. Thus, the coupling of these materials will surely generate a structure with promising properties. Furthermore, it is important to mention that the addition of cobalt in the magnetite structure has been found to improve the coercivity and increase the chemical stability of the solid compared to pure magnetite [27].

*e-mail: tiagoquimicaufrn@gmail.com

There are few studies that use oxidation and reduction steps (controlled synthesis atmosphere) during the preparation of nanocomposite solids [28-31], as it was used in this work. On the other hand, the positive effect of the rotary oven on the formation of the nanocomposites requires further investigation to confirm its viability. The uniform contact of the synthesis atmosphere during the oxidation and/or reduction steps may positively influence on the homogeneity of the obtained phases. Some studies show the positive effect of powder agitation during thermal treatment to obtain alloys or oxides isolated (they are not composites) [12,32,33]. In this work, the positive effect of the rotary oven on structural properties was confirmed in the synthesis of FeCo-$(Fe,Co)_3O_4$ nanocomposite using gelatin route.

2. Materials and Methods

The synthesis of the FeCo-$(Fe,Co)_3O_4$ structure was performed by proteic sol-gel method. The samples were prepared in order to obtain 5 g of FeCo alloy with molar ratio between Fe:Co of 1:1. Initially, they are prepared two different solutions, the first solution consists of 21.1 g of iron (III) nitrate nonahydrate $\{Fe(NO_3)_3 9H_2O\}$ diluted in distilled water and then mixed with 10.6 g of gelatin (GELITA™) under constant thermal agitation to obtain a uniformly dispersed mixture (40°C with rotation of 50 rpm). Concomitantly, the second solution containing 15.2 g of cobalt (II) nitrate hexahydrate $\{Co(NO_3)_2 6H_2O\}$ diluted in distilled water and mixed with 7.6 g of gelatin also under continuous agitation (40°C with rotation of 50 rpm). Subsequently, the solutions containing the gelatin and the nitrates compounds were mixed in a single container and maintained under constant thermal agitation at 100°C until the mixture acquire the consistency of a uniform gel. Afterward, this mixture was placed in a drying oven and remained for 48 h at 100°C. The mass ratio between metal and gelatin was 1:0.5.

The obtained xerogel was macerated, forming a very fine powder, which was calcined in a rotary oven at 700°C for two hours with an air flow of 50mL/min and a rotation of 20 rpm in order to completely oxidize the sample. After, the oxidized solid, still in the rotary oven, is imposed a temperature of 500°C for one hour with a hydrogen flow of 40mL/min and with a rotation of 20 rpm in order to completely reduce the sample to alloy. The alloy is returned to the rotary oven with a mixed flow of nitrogen and air (25mL/min of nitrogen and 5mL/min of air) for 5 min at various temperatures from 400°C in order to control the ratio between FeCo and $(Fe,Co)_3O_4$, since the FeCo alloy oxidizes when placed in the oven at temperatures higher than 400 °C, generating magnetite $(Fe,Co)_3O_4$ with some cobalt atoms in the magnetite lattice.

A little oxidized sample was collected from rotary over for characterization in order to observe the magnetite phase with cobalt atoms in its lattice. Re-oxidation processes were carried out at temperatures of 450 and 500°C in order to analyze what happens with the FeCo alloy when subjected to higher temperatures. The different samples were named CS-X where X is the re-oxidation temperature of the solids. Table 1 shows the conditions used for each material and their names.

Finally, the oxidation, reduction and re-oxidation steps of the sample CS-420 were performed without rotation in order to study the effect of the sample rotation during the oxidation/reduction/re-oxidation process on the microstructure of nanocomposite (crystallite size and microstrain). The powder without rotation was designated CS-420-WR.

Thermogravimetric analysis (TG) was also carried out using a Shimadzu DTA-60H. The measurements were made under air flow (40 mL/min) with a temperature range between 23 and 1000 °C, heating rate of 10 °C/min. The crystallographic structures were determined by X-ray diffraction (XRD) using a X-Pert PRO MPD Panalytical diffractometer for polycrystalline samples. Phase identification was performed through X-Pert HighScore Panalytical software and the JCPDS-ICDD 2003 database [34]. Additionally, Rietveld refinements were done using GSAS software [35] and EXPGUI interface [36], after determining instrumental broadening by means of refining a LaB_6 NIST standard sample. The modified Pseudo-Voigt function (Thompson-Cox-Hastings) was chosen to adjust the profiles of the diffraction peaks for the identified crystalline phases. The width at half height (FWHM) of the peaks was used to calculate the crystallite size using the Scherrer equation [37] and Williamson-Hall plot [38].

The width at half height of the diffraction peak contains information about crystallite size and microstrain. The method developed by G. K. Williamson and W. H. Hall suggests a way to separate these two contributions, the total

Table 1. Samples used and their captions.

Samples	Condition
Pure alloy (FeCo)	Xerogel -> oxidized -> reduced
Pure oxide $\{(Fe,Co)_3O_4\}$	Xerogel -> oxidized
CS-400	Xerogel -> oxidized -> reduced -> re-oxidized (400°C)
CS-415	Xerogel -> oxidized -> reduced -> re-oxidized (415°C)
CS-420	Xerogel -> oxidized -> reduced -> re-oxidized (420°C)
CS-425	Xerogel -> oxidized -> reduced -> re-oxidized (425°C)
CS-430	oxidized -> reduced -> re-oxidized (430°C)
CS-435	oxidized -> reduced -> re-oxidized (435°C)
CS-450	oxidized -> reduced -> re-oxidized (450°C)
CS-500	oxidized -> reduced -> re-oxidized (500°C)

width of the diffraction peak (β) is written as the sum of the contributions, Equation (1):

$$\beta = \beta_S + \beta_C \quad (1)$$

The width relative to the crystallite size (β_C) is obtained by the Scherrer equation, while the width due to strain contribution (β_S) is demonstrated from the Bragg equation [39]. The resulting expression is written according to equation (2).

$$\beta = C\varepsilon tg(\theta) + \frac{k\lambda}{D\cos(\theta)} \quad (2)$$

Where C is a function that depends on the nature of the strain, which can assume as equal to 4, ε is the microstrain, k is the Scherrer constant, λ is the wavelength, D is the crystallite size and θ is the Bragg angle. This is a straight line equation, where its linear coefficient is the inverse of the crystallite size and the angular coefficient is the microstrain [38,39].

Images were obtained with a scanning electron microscopy (SEM-FEG) using a EVO LS15 Carl Zeiss with an energy dispersive X-ray spectrometer (EDS) from Oxford - INCA in order to obtain information concerning the morphology. It was possible to obtain the particle size distribution and the size of the $(Fe,Co)_3O_4$ particles from SEM images.

The samples for transmission electron microscopy (TEM) analyzes were prepared by depositing one drop of the dispersed solid in isopropyl alcohol, previously macerated and sonicated using an ultrafine amorphous carbon film on a copper grid. The images were obtained in the JEOL 2010 TEM microscope of 200 kV. The size of the $(Fe,Co)_3O_4$ particles was also estimated by TEM images.

Fundamental information about the alloy and magnetite was obtained by Mössbauer spectroscopy carried out at room temperature using a ^{57}Co source in a rhodium matrix. The curves were deconvoluted using Normos-90 and PC-Mos II and a least-square fitting routine [40]. Complementing the magnetic analysis, magnetic hysteresis loop was achieved by vibrating sample magnetometry (VSM) at room temperature, with an external magnetic field range between -12 and 12 kOe.

3. Results and Discussion

3.1 Thermal Properties-TG

A result of great interest in the work, as shown in Figure 1, it was the fact that FeCo alloys synthesized by the protein sol-gel route showed a high chemical stability against oxidation. The TG measurement in the pure alloy shows a mass gain at temperatures higher than 400°C. For this reason, a temperature of 400°C was used for the re-oxidation process of the FeCo alloy to obtain a layer of oxide on the alloy. It is worth to emphasize that a mixture of air and N_2 (air diluted in inert atmosphere) was used, since

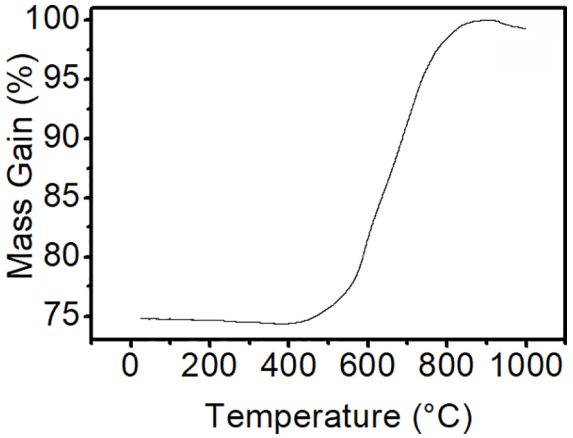

Figure 1. Thermogravimetry Measure (TG) of xerogel under air atmosphere.

it is desired to obtain only a thin layer of oxide on the alloy (nanocomposite), avoiding complete oxidation of the alloy.

3.2 Structural properties (X-ray diffraction)

The X-ray diffraction of the reduced sample shows a single phase of FeCo (ICSD nu. 56273), which has a space group of the Pm-3m type and the lattice parameters of the unit cell obtained through Rietveld refinement are a= 2.85687Å +/- 0.000013 Å. It is observed that they are practically the same comparing with the value obtained in the literature, a = 2.857 Å [14]. The average crystallite size obtained by the Sherrer equation is 75 nm. Figure 2 shows the diffraction profile of the sample as well as the graph generated by the Rietveld refinement and the Williamson Hall plot (W-H). The Rietveld refinement confirms the FeCo phase and the W-H plot indicates a high degree of homogeneity regarding the crystallite size of the sample, indicating that use of the rotary oven favors the reduction of microstrain. The slope of the W-H plot, give information about strain. The larger strain is obtained when the plot is more inclined. Some works show that the strain is inversely proportional to the crystallite size, which is related to the formation of crystallite boundaries. For larger strain values, more crystallite boundaries will exist, causing a decrease in the average crystallite size. On the other hand, a smaller strain value give a fewer crystallite boundaries, causing an increase in the average crystallite size. Therefore, less lattice deformations, cause fewer crystallite boundaries, causing greater homogeneity in the crystallite size distribution. [41-43].

It was also done the diffraction analysis of the fully oxidized sample, Figure 3a, in order to observe separately the oxide phase, and for the refinement a single phase of Magnetite (Fe_3O_4) (ICSD nu. 84611) with space group Pm-3m was used. The refinement confirmed the presence of this phase, whose lattice parameters are a= 8.380770Å +/-0.000878Å, which are compatible with the literature a= 8.375 [26]. For the synthesis of this material the iron:cobalt molar ratio was

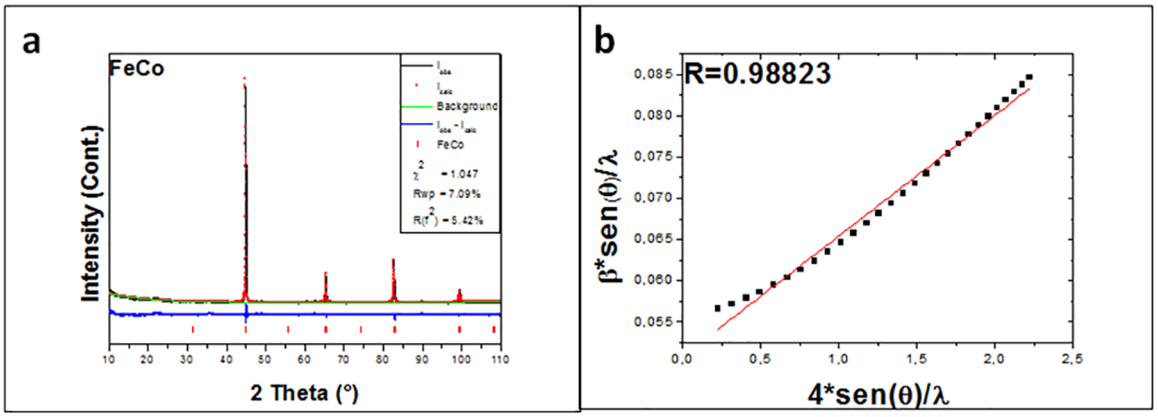

Figure 2. *a)* X-ray diffraction (XRD) measurement and refinement by the Rietveld method of the pure FeCo alloy sample. *b)* Williamson-Hall plot constructed from refinement results.

1:1. It is observed that the diffraction profile of this cobalt oxide is similar to the diffraction profile of the magnetite, considering that the atomic radius of cobalt as well as its scattering factor are very close to the iron. Therefore, it may be verified that this solid is a magnetite doped with cobalt.

The X-ray diffraction of the re-oxidized samples at different temperatures (400, 415, 420, 425, 430 and 435°C) are exposed in Figures 3b, 3c, 3d, 3e, 3f and 3g, respectively. The profiles have two phases, the first related to FeCo alloy (ICSD nu. 56273) and the second concerning magnetite $(Fe,Co)_3O_4$ (ICSD nu. 84611), which this second phase presents a spatial group similar to the FeCo phase, Fd-3m. The lattice parameters obtained using the Rietveld refinement for the FeCo alloy and the magnetite are, a= 2.855092 Å +/- 0.000048 Å and a= 8.392179 Å +/- 0.001190 Å, respectively. It was observed that these values are slightly different from the values found in the literature (2.857 Å for the FeCo phase and 8.375 Å for the Fe_3O_4 phase) [14,26]. For the FeCo phase the explanation is given by the reason that the FeCo alloy is oxidizing, it is not pure, since a phase transition of the FeCo alloy to $(Fe,Co)_3O_4$ is occurring. However, for the second phase, as has been explained previously, a magnetite doped with cobalt atoms is observed, which causes a slight change in the lattice parameter due to the magnetite lattice distortion by the cobalt insertion in its structure. In Table 2 are present the concentrations of both phases as well as the crystallite size of the FeCo phase.

It is observed that the increase of the re-oxidation temperature directly influences the concentration of the magnetite phase, since with a higher re-oxidation temperature it is observed a higher concentration of the magnetite. It is also possible to observe that as the magnetite phase increases the crystallites size of FeCo alloy decreases, indicating that the FeCo alloy is functioning as an iron and cobalt donor source for magnetite. These results are in agreement with the TG profile in Figure 1, since the oxidation of the alloy begins to occur from 400°C.

In order to obtain the average thickness of the $(Fe,Co)_3O_4$ phase using the Rietiveld refinement, a calculation was made using the crystallite sizes of the FeCo phase obtained in the pure alloy sample and in the alloy-oxide mixtures. The crystallite size of the FeCo alloy phase is used for each sample from mixture and the crystallite size for the pure FeCo alloy, taking into account that all the pure alloy samples prior to the re-oxidation process have the same size and also that the $(Fe,Co)_3O_4$ structure prevents growth of the FeCo alloy phase. Therefore, there is a mechanism to estimate the thickness of the $(Fe,Co)_3O_4$, which is in agreement with previously published works [44,45]. The results of this calculation for all the re-oxidized samples are present in Table 3.

X-ray diffraction measurements were performed in two new samples in order to observe what happens with the FeCo alloy at higher temperatures after re-oxidation, Figure 4. It is possible to observe from the identification of phases and consequently after the refinement, the presence of two phases concerning magnetite (Fe_3O_4) and cobalt oxide (Co_3O_4). It is also noted that the structure remains unchanged in the range of 450 and 500°C, increasing only the crystallite size due to the effect of temperature on crystallite sintering, since the diffraction profile is the same for the two solids (relative intensity and position of each peak). The fact that only oxide in the reoxidized solids at 450 and 500°C were observed are in agreement with the TG result, Figure 1, since in this temperature range it is already observed a significant mass gain referring to the complete oxidation of the alloy.

3.3 Morphological properties (SEM and TEM)

High resolution scanning electron microscopy analyzes were performed for two specific samples in order to obtain information related to the morphology of the synthesized materials as well as to estimate the average particle size and

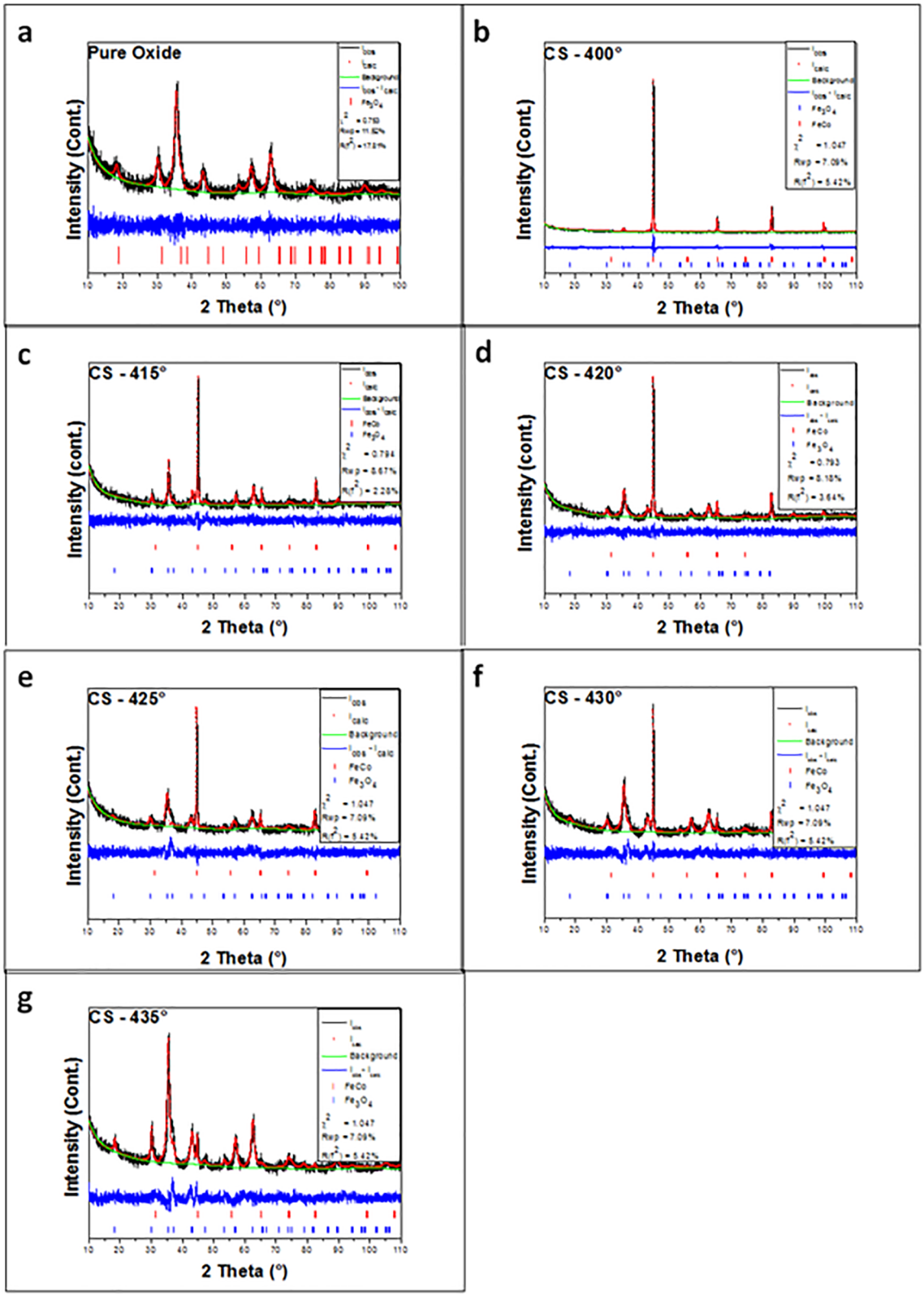

Figure 3. X-ray diffraction (XRD) and refinement by the Rietveld method of the sample: *a)* Pure oxide. *b)* CS-400. c) CS-415. *d)* CS-420. *e)* CS-425. *f)* CS-430. *g)* CS-435.

Table 2. Quantitative results obtained using Rietveld refinement.

Sample	Phase Concentration (%) (FeCo/$(Fe,Co)_3O_4$)	Crystallite size (nm), FeCo alloy
Pure alloy	100/0	145
CS-400	89.81/10.19	107
CS-415	50/50	96
CS-420	42.79/57.21	85
CS-425	31.72/68.28	60
CS-430	18.68/81.32	47
CS-435	3.11/96.88	39
Pure oxide	0/100	-

Table 3. Average thickness of the (Fe,Co)3O4 phase estimated using XRD and Rietveld refinement.

Sample	thickness of the $(Fe,Co)_3O_4$(nm)
CS-400	38
CS-415	48
CS-420	60
CS-425	85
CS-430	98
CS-435	106

compare with the crystallites size obtained by XRD using the Scherrer equation.

A nanoparticle agglomerate is observed in Figures 5a, 5b and 5c, moreover, it is also possible to observe a very thin layer around the nanoparticles, indicating the formation of a thin layer of magnetite on the FeCo alloy. The particle size range is between 100 and 140 nm, as shown in the particle size distribution histogram of Figures 6a, 6b, 6c, respectively. This result is close to the results obtained by Scherrer's equation, considering that the crystallite size was added with the $(Fe,Co)_3O_4$ thickness, as had been predicted. The average $(Fe,Co)_3O_4$ thickness in all images is approximately 30 nm, and this value is also close to the thickness estimated by the Rietveld method in Table 3, which confirms the viability of the XRD calculation (Rietveld refinement). In Figure 5d, an agglomeration of FeCo particles is observed whose average size is 200 nm. The particle size distribution is presented in Figure 6d.

Transmission electron microscopy measurements was a challenge due to the samples were magnetic causing the deflection of the electrons by the field. Figure 7 shows a Transmission Microscopy image of the CS-400 sample. By contrast, it is possible to observe that some particles are covered by a thin layer, confirming the formation of a thin layer of oxide on the alloy. The average particle size is ranging from 110 to 149 nm which is in agreement with the values obtained via Rietveld refinement and SEM-FEG. The average value of the $(Fe,Co)_3O_4$ thickness is approximately 30 nm, which is also in agreement with the values obtained through Rietveld refinement by XRD and FEG-SEM. Therefore, the use of a controlled mixture of air and N_2 at the appropriate temperature is interest to obtain a thin layer of oxide on the alloy (self-assembled FeCo-$(Fe,Co)_3O_4$ nanocomposites) using the gelatin method.

3.4 Magnetic properties (VSM)

The hysteresis curves of the pure FeCo alloy sample, pure oxide, CS-400 and CS-420, are shown in Figure 8a. Comparing the FeCo pure alloy sample with the pure oxide, it can be seen that the pure alloy has a slightly higher saturation magnetization twice compared to pure oxide, as expected. On the other hand, the coercivity of the pure oxide sample is greater than the pure alloy, confirming that FeCo alloy is a soft magnetic materials and $(Fe,Co)_3O_4$ is a hard magnetic material. It is also possible to observe that increasing the amount of oxide in the samples CS-400 and CS-420 compared to the pure alloy provides a decrease in the saturation magnetization of the material. It is also possible to

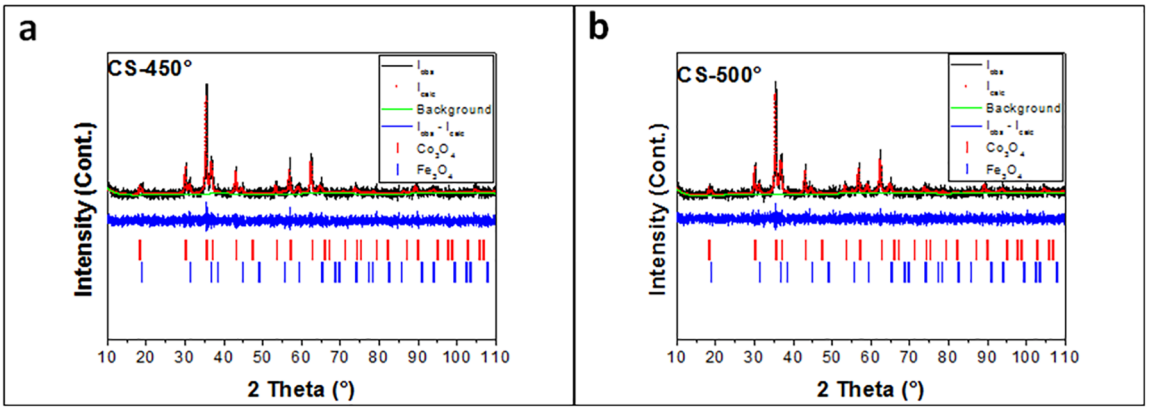

Figure 4. X-ray diffraction (XRD) measurement and Rietveld refinement of the samples: *a)* CS-450. *b)* CS-500.

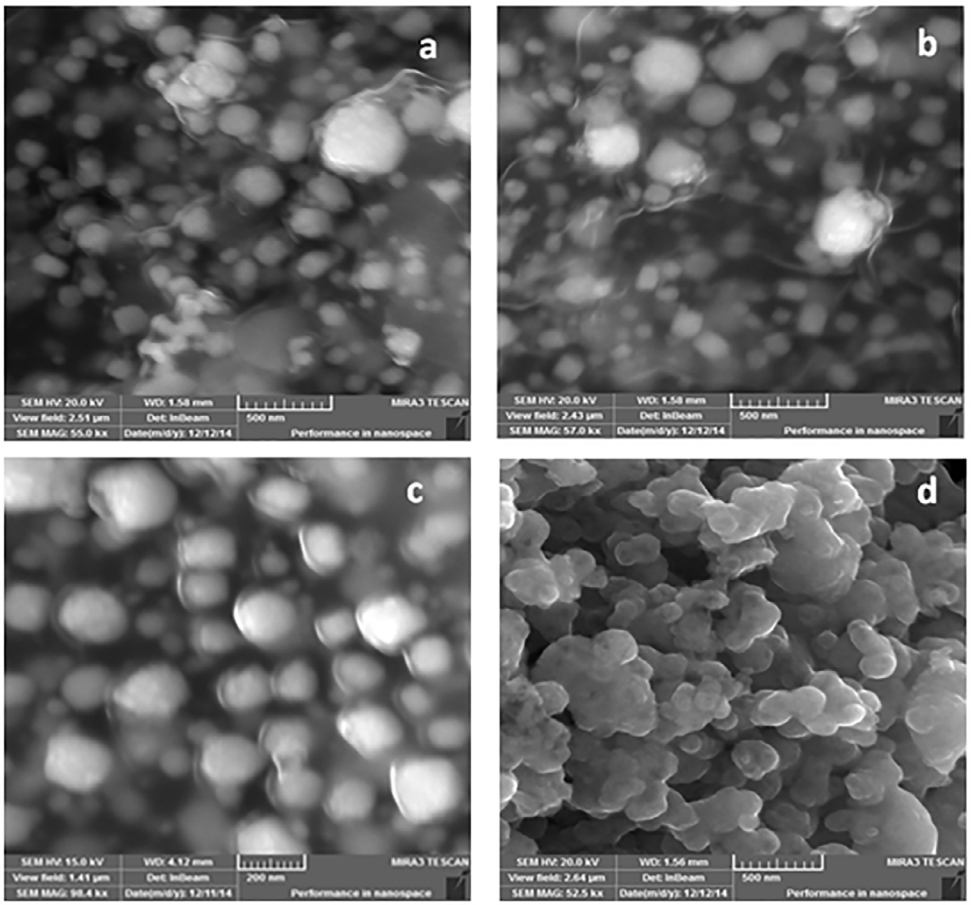

Figure 5. Scanning electron microscopy images for the sample CS-400.

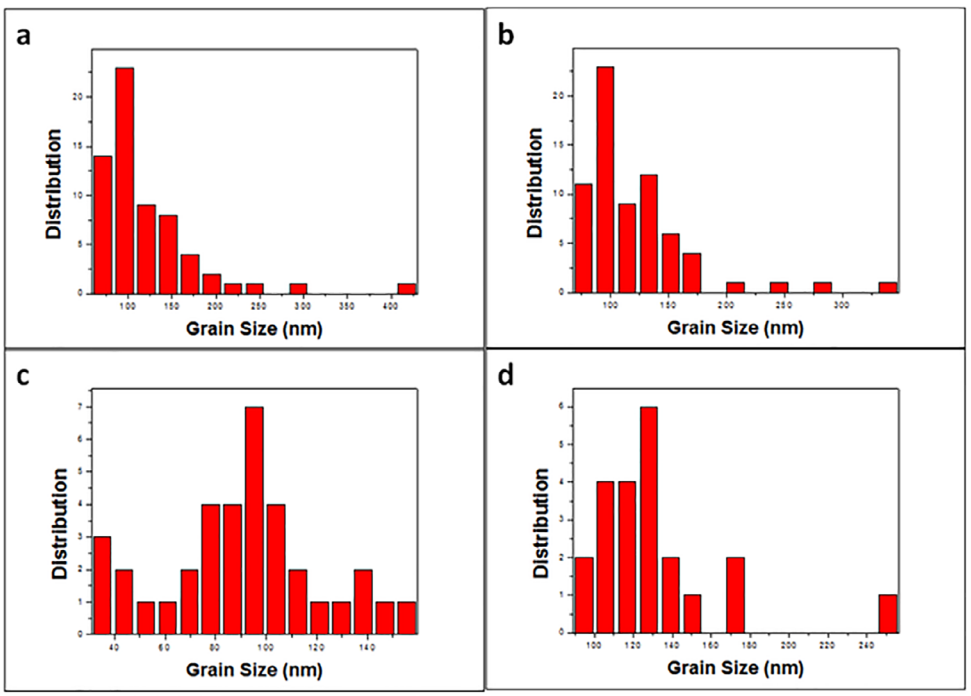

Figure 6. Particle size distributions of the sample CS-400 obtained by FEG-SEM.

observe an increase in coercivity (zoom in the central region of the hystereses). The saturation magnetization values of the solids are present in Table 4.

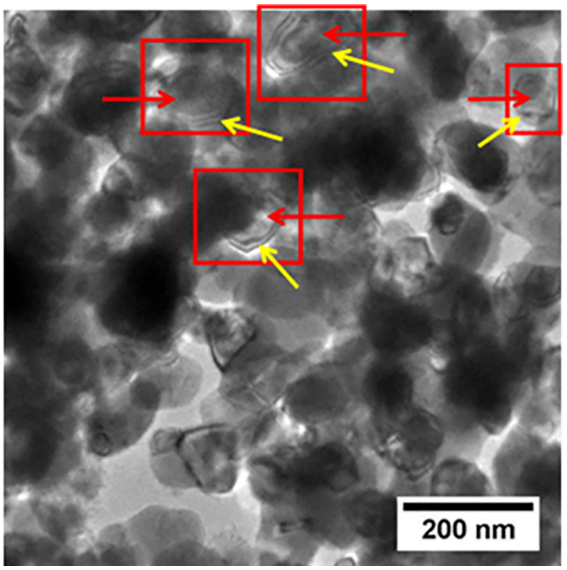

Figure 7. Transmission electron microscopy images for the CS-400 sample. The red arrows represent the FeCo alloy while the yellow ones represent the $(Fe,Co)_3O_4$ phase (magnetite doped with Co).

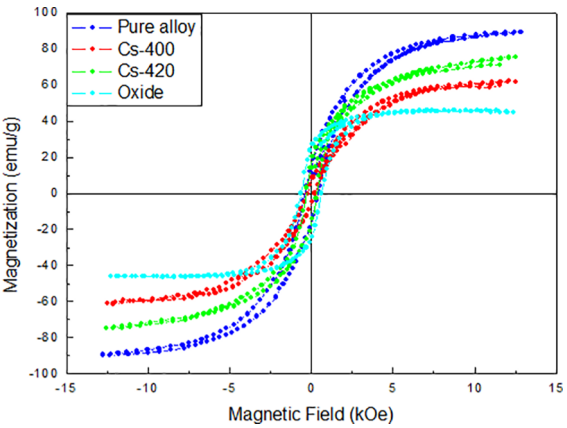

Figure 8. Vibrating sample magnetometer measurement done at room temperature for the sample: pure alloy, CS-400, CS-420 and pure oxide.

Table 4. Saturation magnetization (Ms), ratio between the remaining magnetization Mr and Ms (Mr/Ms), coercive field (Hc) for oxide, pure alloy, CS-400 and CS-420 samples.

Sample	Ms (emu/g)	Mr/Ms	Hc (Oe)
Oxide	45.10	0.55	572
Pure alloy	89.50	0.17	392
CS-400	61.76	0.10	240
CS-420	75.59	0.22	333

Another effect that has been observed is the increase of the Mr/Ms ratio value (Mr: remanent magnetization and Ms: saturation magnetization), when the re-oxidation temperature is higher, consequently when the oxide concentration is higher. Table 4 presents the ratios for the oxide, pure alloy, CS-400 and CS-420 samples. It was obtain a Mr/Ms ratio of 0.55 for the pure oxide. This value agrees with the theoretically predicted for a system containing single-domains magnetic nanoparticles with uniaxial anisotropy.

It is observed that there are no jumps for all the magnetization curves, thus, it is a curve similar to a hysteresis obtained for a single phase, indicating that the magnetization for both phases are working cooperatively and the fields generated by both materials are working together and are not canceled in any way [46]. This fact may be explained by the exchange spring magnetic behavior. Therefore, the reoxidized materials have both high saturation magnetization and high coercivity, which is different from the isolated materials.

Thus, the data of magnetic characterization indicate that all of the nanocomposites containing FeCo alloy and $(Fe,Co)_3O_4$ exhibit ferromagnetic behavior. These nanocomposites consist of magnetically hard and soft phases where there is some degree of magnetic exchange coupling between the FeCo alloy and magnetite domains.

3.5 Chemical environment of Fe (Mossbauer spectroscopy)

Mössbauer spectroscopy was done at room temperature in the pure FeCo and in the CS-400 and CS-420 re-oxidized samples. The results are shown in Figures 9a, 9b and 9c, respectively. It is possible to observe only one sextet and one singlet for the pure alloy sample, showing that the alloy has a great homogeneity related to the chemical environment of iron and the iron is only in one site according to the obtained hyperfine parameters presented in Table 5, which confirms the body-centered cubic structure observed in X-ray diffraction (Figures 2 and 3).

On the other hand, in the spectrum of the re-oxidized samples, it is possible to observe a doublet in the two samples whose hyperfine parameters are shown in Table 5, and the values are equivalent to those found in the Fe_3O_4 phase (magnetite) [47]. Furthermore, a single sextet was observed in the CS-400 sample, indicating that the iron is in only one site concerning the structure BCC, while in the CS-420 sample, two sextets were observed, indicating that iron is present in two different sites, the first BCC and the second the FCC (face-centered cubic structure). It is observed that the spectra obtained by Mössbauer spectroscopy corroborate with the same phases identified by X-Ray Diffraction and confirmed by the Rietveld refinements. Therefore, the Mossbauer results

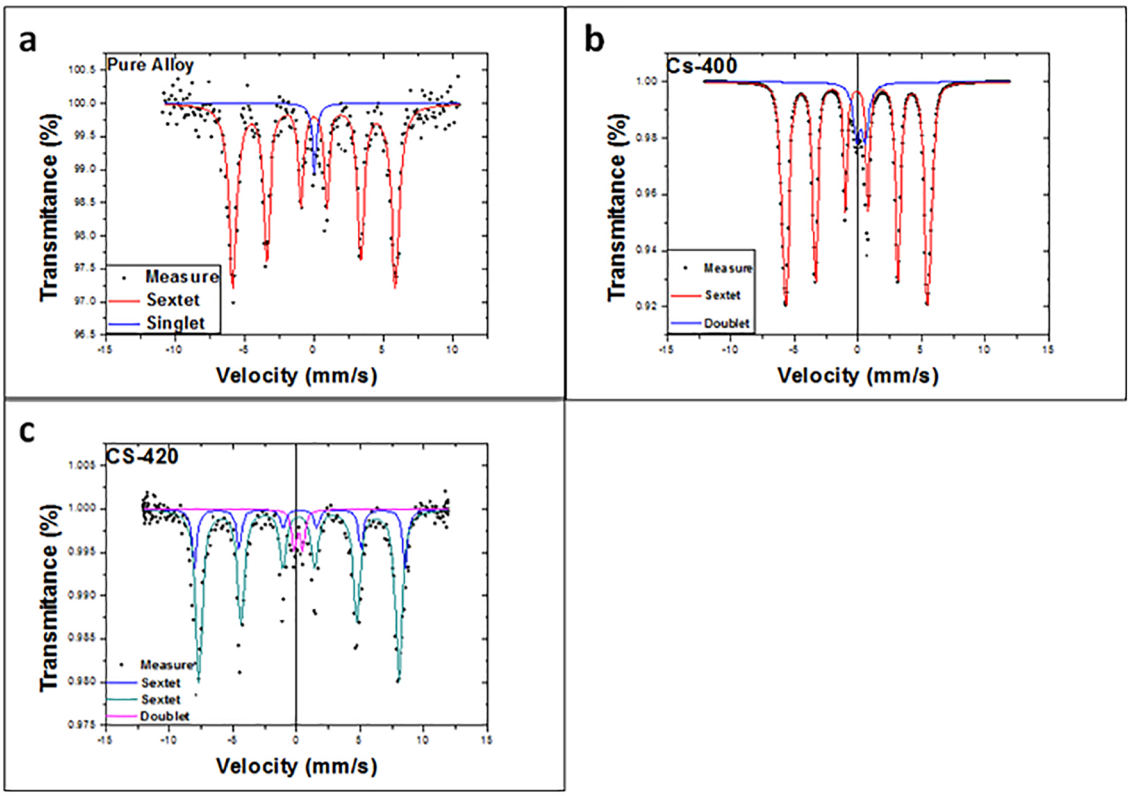

Figure 9. Mössbauer spectroscopy results of the sample: a) Pure alloy. b) CS-400. c) CS-420.

Table 5. Hyperfine parameters obtained from Mössbauer spectroscopy.

Sample	Type	HF (T)	QS (mm/s)	IS (mm/s)	Área (%)
Pure alloy	Sextet	36.5164	0.025	0.0132	94.97
	Singlet	-	-	0.0489	5.03
CS-400	Sextet	30.0	0.00	-0.11	95.63
	Doublet	-	0.60	0.21	4.37
CS-420	Sextet	51.435	-0.02	0.37	19.3
	Sextet	48.868	0.00	0.29	74.6
	Doublet	-	0.68	0.26	6.1

also confirm that a small amount of oxide was formed on the alloy after the re-oxidation process as already confirmed in previous results (XRD, SEM, TEM and VSM).

3.6 Effect of the powder rotation on the formation of FeCo-$(Fe,Co)_3O_4$ structure

It was selected the sample CS-420 in order to analyze the influence of the powder rotation employed during the synthesis steps on the homogeneity of the obtained phases. For comparison, it was redone the oxidation/reduction/reoxidation steps without rotation (CS-420-WR sample).

The XRD results of the solids with and without rotation are presented in Figure 10-a and the Williamson-Hall plot in Figure 10-b. Comparing these results with the data obtained for the solid CS-420 with rotation, it was observed that the rotation of the sample is essential for the formation of a thin layer of oxide (magnetite) on the FeCo alloy, considering that the alloy was not observed in the sample without rotation (Fig. 10-a). The powder without rotation indicated the formation of magnetite (ICSD nu. 56273) and metallic cobalt (ICSD nu. 56273), indicating that the alloy was not formed in this case.

In addition, from the Williamson-Hall plot (Figure 10-b), it was noted that the rotation of the powder during synthesis using the rotary oven produces particles with low microstrain and superior homogeneity, since showed a lower value of microstrain and a better fit of data points (higher correlation coefficient). Thus, the use of a rotary oven is essential to obtain solids with low defect density, high purity and better homogeneity related to the crystallite size.

4. Conclusions

It was possible to obtain a magnetically exchange coupled FeCo-$(Fe,Co)_3O_4$ structure by proteic sol-gel method using a rotary oven. It was also observed that within the magnetite structure there were some cobalt atoms completing the magnetite lattice due to the fact that the cobalt atoms have an atomic radius, as well as an electronic distribution and the scattering factors very close to the iron atom, allowing its

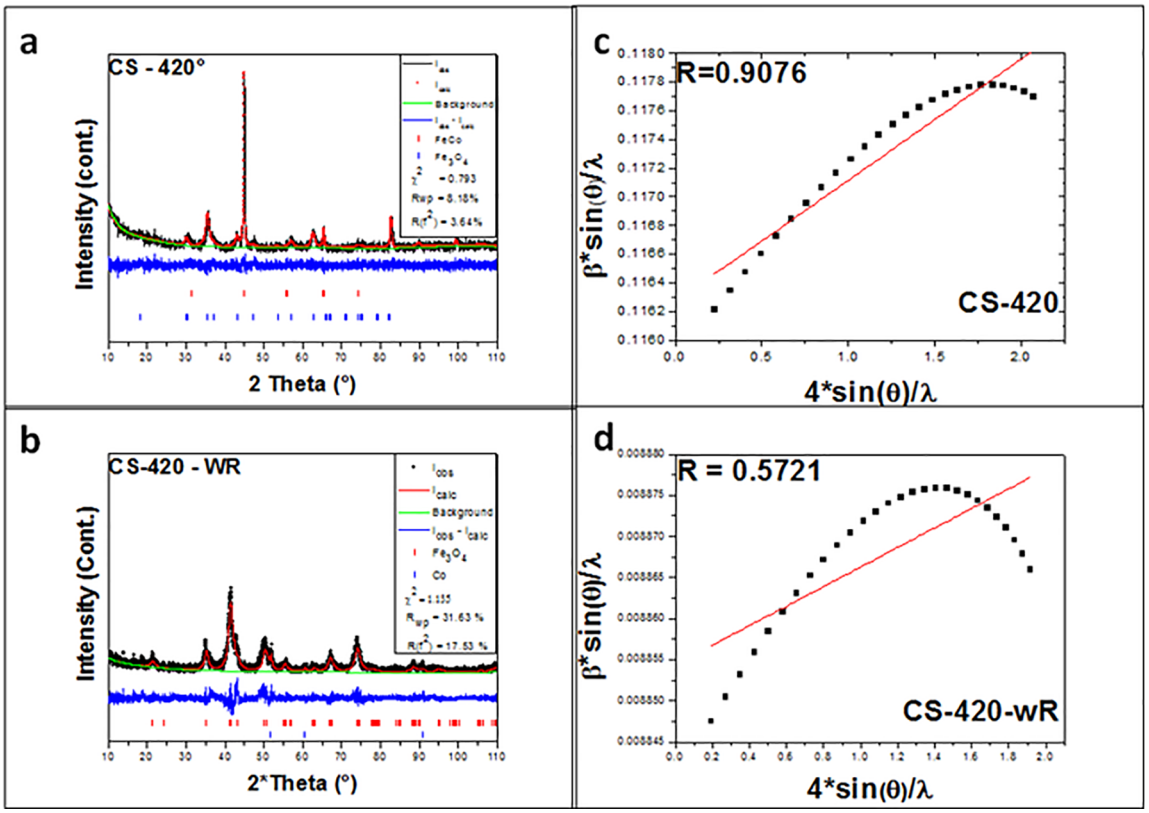

Figure 10. *a)* Diffractograms and *b)* Williamson-Hall plot for the solid CS-420 with and without rotation.

replacement. A magnetic exchange spring may be occurring in the FeCo-$(Fe,Co)_3O_4$ structure according to the VSM results.

Increasing the re-oxidation temperature occurs an increase in the concentration of the magnetite phase as well as a decrease of the $(Fe,Co)_3O_4$ radius, therefore, it is possible to control the $(Fe,Co)_3O_4$ phase concentration as well as the $(Fe,Co)_3O_4$ radius through the temperature and the correct choice of the N_2 and air flow. The rotary oven employed in the synthesis is essential for the formation of FeCo-$(Fe,Co)_3O_4$ structure with low microstrain and high homogeneity related to the crystallite size.

5. Acknowledgments

The authors would like to thank Brazilian funding agencies CNPq and CAPES for financial support. Also, GELITA Company for providing the edible gelatin, State University of Rio Grande do Norte, Mossoró campus, for FEG-SEM and VSM analysis. Luelc Souza for the transmission electron microscopy (TEM) images.

6. References

1. Kubo AM, Gorup LF, Amaral LS, Rodrigues-Filho E, de Camargo ER. Heterogeneous Microtubules of Self-assembled Silver and Gold Nanoparticles Using Alive Biotemplates. Materials Research. 2018;21(4):e20170947.

2. Singh H, Yadav KL. Synthesis and study of structural, dielectric, magnetic and magnetoelectric characterization of BiFeO3-NiFe2O4 nanocomposites prepared by chemical solution method. Journal of Alloys and Compounds. 2014;585:805-810.

3. Vieira KO, Panzera TH, Ferrari JL, Schiavon MA. Nanocomposites Based on Polyelectrolytes-Multiwalled Carbon Nanotubes Coated with a Silica Shell. Materials Research. 2018;21(6):e20180291.

4. Yang YJ, Li W. Hierarchical Ni-Co double hydroxide nanosheets on reduced graphene oxide self-assembled on Ni foam for high-energy hybrid supercapacitors. Journal of Alloys and Compounds. 2019;776:543-553.

5. Elmahdy M, Abouelmagd G, Mazen AAE. Microstructure and Properties of Cu-ZrO2 Nanocomposites Synthesized by in Situ Processing. Materials Research. 2018;21(1):e20170387.

6. de Oliveira ASK, Paulista APF, de Alencar AEV, Braga TP. Gelatin Template Synthesis of Aluminum Oxide and/or Silicon Oxide Containing Micro/Mesopores Using the Proteic Sol-Gel Method. Journal of Nanomaterials. 2017;2017:2504796.

7. Pourroy G, Valles-Minguez A, Jurca IS, Meny C, Viart N, Panissod P. Synthesis and properties of Fe0-Co0/Co-magnetite composites under hydrothermal conditions. Journal of Alloys and Compounds. 2002;333(1-2):296-301.

8. Tyan HL, Liu YC, Wei KH. Thermally and Mechanically Enhanced Clay/Polyimide Nanocomposite via Reactive Organoclay. Chemistry of Materials. 1999;11(7):1942-1947.

9. Froba M, Köhn R, Bouffaud G, Richard O, van Tendeloo G. Fe2O3 Nanoparticles within Mesoporous MCM-48 Silica:?In Situ Formation and Characterization. Chemistry of Materials. 1999;11(10):2858-2865.

10. Osso D, Tillement O, Le Caer G, Mocellin A. Alumina-alloy nanocomposite powders by mechanosynthesis. Journal of Materials Science. 1998;33(12):3109-3119.

11. Estournès C, Cornu N, Guille JL. Reduction of copper in soda-lime-silicate glass by hydrogen. Journal of Non-Crystalline Solids. 1994;170(3):287-294.

12. Jay JP, Jurca IS, Pourroy G, Viart N, Mény C, Panissod P. 59Co NMR study in Co-Fe alloys/Co magnetite composites. Solid State Sciences. 2001;3(3):301-308.

13. Lakamp S, Pourroy G. Composite-materials made of spinel (CoyFe3-yO4) and cobalt-iron (CoxFe1-x) - parametrization of the synthetic route. European Journal of Solid State and Inorganic Chemistry. 1997;34(3):295-308.

14. Braga TP, Dias DF, de Sousa MF, Soares JM, Sasaki JM. Synthesis of air stable FeCo alloy nanocrystallite by proteic sol-gel method using a rotary oven. Journal of Alloys and Compounds. 2015;622:408-417.

15. Helminger M, Wu B, Kollmann T, Benke D, Schwahn D, Pipich V, et al. Synthesis and Characterization of Gelatin-Based Magnetic Hydrogels. Advanced Functional Materials. 2014;24(21):3187-3196.

16. Zhang L, Wang Z, Xu Y. Superior high-temperature magnetic softness for Al-doped FeCo-based nanocrystalline alloys. Journal of Non-Crystalline Solids. 2018;481:148-151.

17. Murugaiyan P, Abhinav A, Verma R, Panda AK, Mitra A, Baysakh S, et al. Influence of Al addition on structural, crystallization and soft magnetic properties of DC Joule annealed FeCo based nanocrystalline alloys. Journal of Magnetism and Magnetic Materials. 2018;448:66-74.

18. Miller KJ, Colletti A, Papi PJ, McHenry ME. Fe-Co-Cr nanocomposites for application in self-regulated rf heating. Journal of Applied Physics. 2010;107(9):09A313.

19. Yang F, Chen H, Liu D, Xiong P, Li W, Chen X. The microstructure and magnetic properties of FeCo@SiO2 core-shell nanoparticles synthesized by using a solution method. Journal of Alloys and Compounds. 2017;728:1153-1156.

20. Martínez Sánchez H, Zamora Alfonso LE, Trujillo Hernandez JS, Pérez Alcázar GA. Evidence of exchange coupling in t-MnAlC/FeCo system. Journal of Magnetism and Magnetic Materials. 2019;473:221-227.

21. Koike M, Hisada Y, Wang L, Li D, Watanabe H, Nakagawa Y, et al. High catalytic activity of Co-Fe/a-Al2O3 in the steam reforming of toluene in the presence of hydrogen. Applied Catalysis B: Environmental. 2013;140-141:652-662.

22. Qiu FY, Wang YJ, Wang YP, Li L, Liu G, Yan C, et al. Dehydrogenation of ammonia borane catalyzed by in situ synthesized Fe-Co nano-alloy in aqueous solution. Catalysis Today. 2011;170(1):64-68.

23. Wang L, Hisada Y, Koike M, Li D, Watanabe H, Nakagawa Y, et al. Catalyst property of Co-Fe alloy particles in the steam reforming of biomass tar and toluene. Applied Catalysis B: Environmental. 2012;121-122:95-104.

24. Cheng Y, Ji G, Li Z, Lv H, Liu W, Zhao Y, et al. Facile synthesis of FeCo alloys with excellent microwave absorption in the whole Ku-band: Effect of Fe/Co atomic ratio. Journal of Alloys and Compounds. 2017;704:289-295.

25. Barbosa FF, Pergher SBC, Braga TP. Synthesis of highly stable FeCo alloy encapsulated in organized carbon from ethylbenzene using H2, CH4, C2H4 generated in situ. Journal of Alloys and Compounds. 2019;772:625-636.

26. Blaney L. Magnetite (Fe3O4): Properties, Synthesis, and Applications. Lehigh Review. 2007;15(5):33-81.

27. Wang Q, Wu A, Yu L, Liu Z, Xu W, Yang H. Nanocomposites of Iron-Cobalt Alloy and Magnetite: Controllable Solvothermal Synthesis and Their Magnetic Properties. Journal of Physical Chemistry C. 2009;113(46):19875-19882.

28. Yang B, Li X, Guo R, Yu R. Oxidation fabrication and enhanced soft magnetic properties for core-shell FeCo/CoFe2O4 micron-nano composites. Materials & Design. 2017;121:272-279.

29. Lu M, Liu M, Wang L, Xu S, Zhao J, Li H. Structural and magnetic properties of CoFe2O4/CoFe2/SiO2 nanocomposites with exchange coupling behavior. Journal of Alloys and Compounds. 2017;690:27-30.

30. Safi R, Ghasemi A, Shoja-Razavi R, Tavoosi M. Development of novel exchange spring magnet by employing nanocomposites of CoFe2O4 and CoFe2. Journal of Magnetism and Magnetic Materials. 2016;419:92-97.

31. Du G, Wang S. Synthesis of magnetically exchange coupled CoFe2O4/CoFe2 core/shell composite particles through spray pyrolysis. Journal of Alloys and Compounds. 2017;708:600-604.

32. Almeida JMA, Meneses CT, de Menezes AS, Jardim RF, Sasaki JM. Synthesis and characterization of NiMn2O4 nanoparticles using gelatin as organic precursor. Journal of Magnetism and Magnetic Materials. 2008;320(14):e304-e307.

33. Nogueira NAS, da Silva EB, Jardim PM, Sasaki JM. Synthesis and characterization of NiAl2O4 nanoparticles obtained through gelatina. Materials Letters. 2007;61(25):4743-4746.

34. Bayliss P. ICDD Grant-in-Aid. Calgary: University of Calgary; 1990.

35. Larson AC, Von Dreele RB. General Structure Analysis System (GSAS). Los Alamos: Los Alamos National Laboratory; 2004.

36. Toby BH. EXPGUI, a graphical user interface for GSAS. Journal of Applied Crystallography. 2001;34(Pt 2):210-213.

37. Patterson AL. The Scherrer Formula for X-Ray Particle Size Determination. Physical Review. 1939;56(10):978-982.

38. Williamson GK, Hall WH. X-ray line broadening from filed aluminium and wolfram. Acta Metallurgica. 1953;1(1):22-31.

39. Izumi F, Ikeda T. Implementation of the Williamson-Hall and Halder-Wagner Methods into RIETAN-FP. Annual Report of the Advanced Ceramics Research Center of Nagoya Institute of Technology. 2015;3(3):33-38.

40. Brand RA. Normos Mössbauer Fitting Program. Dortmund: TU Dortmund University; 2002.

41. Kherchachi IB, Attaf A, Said H, Bouhdjer A, Bendjedidi H, Benkhetta Y, et al. Structural, optical and electrical properties of Snx Sy thin films grown by spray ultrasonic. Journal of Semiconductors. 2016;37(3):032001.

42. Quah HJ, Cheong KY, Hassan Z, Lockman Z, Jasni FA, Lim WF. Effects of Postdeposition Annealing in Argon Ambient on Metallorganic Decomposed CeO2 Gate Spin Coated on Silicon. Journal of the Electrochemical Society. 2010;157(1):H6-H12.

43. Dolatmoradi A, Raygan S, Abdizadeh H. Mechanochemical synthesis of W-Cu nanocomposites via in-situ co-reduction of the oxides. Powder Technology. 2013;233:208-214.

44. Camardese J, McCalla E, Abarbanel DW, Dahn JR. Determination of Shell Thickness of Spherical Core-Shell NixMn1-x(OH)2 Particles via Absorption Calculations of X-Ray Diffraction Patterns Journal of the Electrochemical Society. 2014;161(5):A814-A820.

45. Hui C, Shen C, Tian J, Bao L, Ding H, Li C, et al. Core-shell Fe3O4@SiO2 nanoparticles synthesized with well-dispersed hydrophilic Fe3O4 seeds Nanoscale. 2011;3(2):701-705.

46. Leite GCP, Chagas EF, Pereira R, Prado RJ, Terezo AJ, Alzamora M, et al. Exchange coupling behavior in bimagnetic CoFe2O4/CoFe2 nanocomposite. Journal of Magnetism and Magnetic Materials. 2012;324(18):2711-2716.

47. Makki R, Steinbock O. Nonequilibrium synthesis of silica-supported magnetite tubes and mechanical control of their magnetic properties. Journal of the American Chemical Society. 2012;134(37):15519-15527.